

# Real-Time Feature Extraction from Electrocochleography with Impedance Measurements during Cochlear Implantation using Linear State-Space Models

Raphael R. Andonie<sup>1,2</sup>, Wilhelm Wimmer<sup>1,2,3</sup>, Reto A. Wildhaber<sup>4,5</sup>, Marco Caversaccio<sup>1,2</sup>, and Stefan Weder<sup>1</sup>

**Abstract**—Electrocochleography (ECoChG) is increasingly used to monitor the inner ear function of cochlear implant (CI) patients during surgery. Current ECoChG-based trauma detection shows low sensitivity and specificity and depends on visual analysis by experts. Trauma detection could be improved by including electric impedance data recorded simultaneously with the ECoChG. However, combined recordings are rarely used because the impedance measurements produce artifacts in the ECoChG.

In this study, we propose a framework for automated real-time analysis of intraoperative ECoChG signals using Autonomous Linear State-Space Models (ALSSMs).

We developed ALSSM based algorithms for noise reduction, artifact removal, and feature extraction in ECoChG. Feature extraction includes local amplitude and phase estimations and a confidence metric over the presence of a physiological response in a recording. We tested the algorithms in a controlled sensitivity analysis using simulations and validated them with real patient data recorded during surgeries.

The results from simulation data show that the ALSSM method provides improved accuracy in the amplitude estimation together with a more robust confidence metric of ECoChG signals compared to the state-of-the-art methods based on the fast Fourier transform (FFT). Tests with patient data showed promising clinical applicability and consistency with the findings from the simulations.

We showed that ALSSMs are a valid tool for real-time analysis of ECoChG recordings. Removal of artifacts using ALSSMs enables simultaneous recording of ECoChG and impedance data. The proposed feature extraction method provides the means to automate the assessment of ECoChG. Further validation of the algorithms in clinical data is needed.

## I. INTRODUCTION

COCHLEAR IMPLANTATION is a highly effective treatment for patients suffering from severe-to-profound hearing loss. For cochlear implant (CI) patients, an electrode array

is placed in the inner ear to stimulate the auditory nerve fibers to transmit sound from an external microphone to the brain. To optimize the surgical and audiological outcome, it is crucial to preserve cochlear structure and function during implantation [1]–[4].

Electrocochleography (ECoChG) is increasingly used to monitor cochlear health during cochlear implantation [5]–[14]. ECoChG measures cochlear biopotentials in response to an acoustic stimulus. Using pure tone stimulation (i.e., sinusoidal stimulus), responses are commonly recorded in pairs, consisting of a rarefaction (RAR) and condensation (CON) response. RAR and CON refer to the polarity of the longitudinal pressure wave of the applied stimulus. Different response components can be derived from these ECoChG signals, which are suggested to originate from different neurosensory sources within the cochlea [15]. The cochlear microphonic (CM) mainly indicates the function of the outer hair cells (OHC) and is an electrical reflection of the acoustic stimulus [16]. It is considered the ECoChG component with the most predictive power regarding cochlear health [11], [17]–[20]. To measure the CM, the difference signal (DIF) between CON and RAR is analyzed. However, acoustic harmonics in the measurements prevents perfect separation of the single response component [11], [21], [22].

We refer to real-time ECoChG (rt-ECoChG) as an ECoChG that was continuously recorded and instantly processed during surgery [10]. A typical intracochlear rt-ECoChG measurement recorded by the CI's most apical electrode during surgery is shown in Figure 1. Individual *epochs* are composed of several buffers, which are acquired from repeatedly recorded responses. In this way, response pairs (CON and RAR) are recorded at a repetition rate of 1.25Hz. We obtain the DIF signal by subtracting the RAR from the CON responses. The continuous recording generates a sequence of epochs, referred to as the rt-ECoChG *measurement*. By extracting features (e.g. CM amplitude or phase) from the epochs, *feature traces* are created over the duration of a measurement. We refer to the collection of different feature traces as the *insertogram*.

Studies have found a significant correlation between changes in CM amplitude during CI electrode insertion and postoperative preservation of residual hearing [4], [5], [23], [24]. However, existing methods for trauma detection show

<sup>1</sup> Department of ENT, Head and Neck Surgery, Inselspital, Bern University Hospital, University of Bern, Switzerland

<sup>2</sup> ARTORG Center for Biomedical Engineering Research, Bern University Hospital, University of Bern, Switzerland

<sup>3</sup> Technical University of Munich, Germany; TUM School of Medicine, Klinikum rechts der Isar, Department of Otorhinolaryngology

<sup>4</sup> Institute for Medical Engineering and Medical Informatics, University of Applied Sciences and Arts Northwestern Switzerland, Muttenz, Switzerland

<sup>5</sup> Signal and Information Processing Laboratory (ISI), ETH Zurich, Zurich, Switzerland

This work was supported by Cochlear Ltd., Melbourne, Australia. Corresponding author: Wilhelm Wimmer (wilhelm.wimmer@unibe.ch)

low sensitivity and specificity and are limited to functional preservation in patients with substantial residual hearing [13], [19]. Moreover, the current gold standard is the visual inspection of the ECoHG signals by an expert, which prevents the integration of the analysis into an automated software [25], [26]. A promising strategy to achieve more reliable automatic trauma detection is to include more data such as the electrical impedance of the CI electrodes in the analysis in addition to the rt-ECoHG amplitude features [27]–[32]. Electrical impedance data provides information about the electrode-tissue interface, including the electrode-electrolyte interface and the surrounding tissue resistance [33]. The increased complexity due to the simultaneous measurement of rt-ECoHG and impedance in real time (rt-impedance) as well as the extraction of more signal features poses new challenges to the signal processing methods applied. In this paper, we present a new method for real-time analysis of intraoperative rt-ECoHG using autonomous linear state-space models (ALSSMs), enabling the simultaneous measurement of rt-impedance data. Our ALSSM based algorithms address a broad range of signal processing tasks such as artifact removal, filtering and feature extraction [34].

## II. MATERIALS AND METHODS

In this section, we briefly introduce the basics of ALSSM and how we use it to create algorithms for processing rt-ECoHG. In addition, we show how we tested the performance of these new algorithms using simulation data and how we validated them in a visual proof of concept using exemplary real patient data. For comparison, we also applied an established standard method to both the simulations and the patient data.

### A. ALSSMs as Signal Models

Model-based signal processing methods are well suited for the analysis of biological signals, as they allow to incorporate a priori knowledge of the signal physiology. ALSSMs enable the efficient online implementation of such model-based algorithms [34]–[36]. The ALSSMs in this study were implemented using the open source software library *lmlib* [37].

Discrete-time ALSSMs can generate functions such as polynomials, exponentials, and sinusoids, as well as linear combinations of those [38]. An ALSSM of order  $N$  is given by the recursive state equation and the output equation

$$x_{i+1} = Ax_i \quad (1)$$

$$m_i = cx_i \quad (2)$$

with state transition matrix  $A \in \mathbb{R}^{N \times N}$ , output vector  $c \in \mathbb{R}^{1 \times N}$ , state vector  $x_i \in \mathbb{R}^N$ , model output  $m_i \in \mathbb{R}$ , and time index  $i \in \mathbb{Z}$ .

Substitution of  $x_i$  in (2) with (1) leads to

$$m_i(x_0) = cA^i x_0 \quad (3)$$

with initial state vector  $x_0$ . Note that the output of a model, defined by  $A$  and  $c$ , is fully determined by the initial state  $x_0$ . For the sake of simplicity, we subsequently denote this initial state  $x_0$  as  $x$ .

### B. Localized ALSSM to Signal Fitting

The best approximation of an observed signal  $y \in \mathbb{R}^K$  with  $K$  samples under the premise of a particular signal model is defined as the model output  $m(\hat{x})$  yielding a minimal *cost* with respect to the squared error. For local signal approximation with ALSSMs in the interval  $i \in \{a, \dots, b\}$ ,  $a, b \in \mathbb{Z}$ , a *cost segment*

$$J_a^b(x, k; \gamma) = \sum_{i=k+a}^{k+b} \gamma^{i-k} (y_i - cA^{i-k}x)^2 \quad (4)$$

is used at filter index  $k \in \mathbb{Z}$  [34].  $\gamma^{i-k}$  adds a left- or right-sided exponentially decaying window to the cost term. By rewriting (4) in the form

$$J_a^b(x, k; \gamma) = x^T W_k x - 2x^T \xi_k + \kappa_k \quad (5)$$

with substitutes

$$W_k = \sum_{i=k+a}^{k+b} \gamma^{i-k} (A^{i-k})^T c^T c A^{i-k} \in \mathbb{R}^{N \times N} \quad (6)$$

$$\xi_k = \sum_{i=k+a}^{k+b} \gamma^{i-k} y_i (A^{i-k})^T c^T \in \mathbb{R}^N \quad (7)$$

$$\kappa_k = \sum_{i=k+a}^{k+b} \gamma^{i-k} y_i^2 \in \mathbb{R} \quad (8)$$

the actual computation can be performed in a sliding window manner and with minimum computational effort as a recursive least squares algorithm. In this case, the decaying window is essential to ensure numerical stability. Finally, the optimal state is given by

$$\hat{x}_k = \operatorname{argmin}_{x \in \mathbb{R}^N} J_a^b(x, k; \gamma) \quad (9)$$

$$= W_k^{-1} \xi_k. \quad (10)$$

as showed in [34].

### C. Constrained Parameter Optimization

To achieve a desired behavior of the model, in many cases it is advantageous to restrict the space of solutions for (10) from  $\mathbb{R}^N$  to a subspace of it. For a  $M$  dimensional subspace, we introduce the linear constraint

$$x = Hv \quad (11)$$

with the constraint matrix  $H \in \mathbb{R}^{N \times M}$ . The minimization problem (10) then modifies to

$$\hat{v}_k = \operatorname{argmin}_{v \in \mathbb{R}^M} J_a^b(Hv, k; \gamma) \quad (12)$$

$$= (H^T W_k H)^{-1} H^T \xi_k. \quad (13)$$

### D. Composite Cost and Model Superposition

Multiple cost segments can be combined to achieve more complex filter characteristics. Such a combination of cost segments is called a *composite cost*, of which there are several variants [34].

To subsequently join  $P$  cost segments with individual decay factors  $\gamma^{(p)}$  and interval borders  $a_p, b_p$ , we get the summed cost

$$\tilde{J}(x, k) = \sum_{p=1}^P J_{a_p}^{b_p}(x, k; \gamma^{(p)}) \quad (14)$$

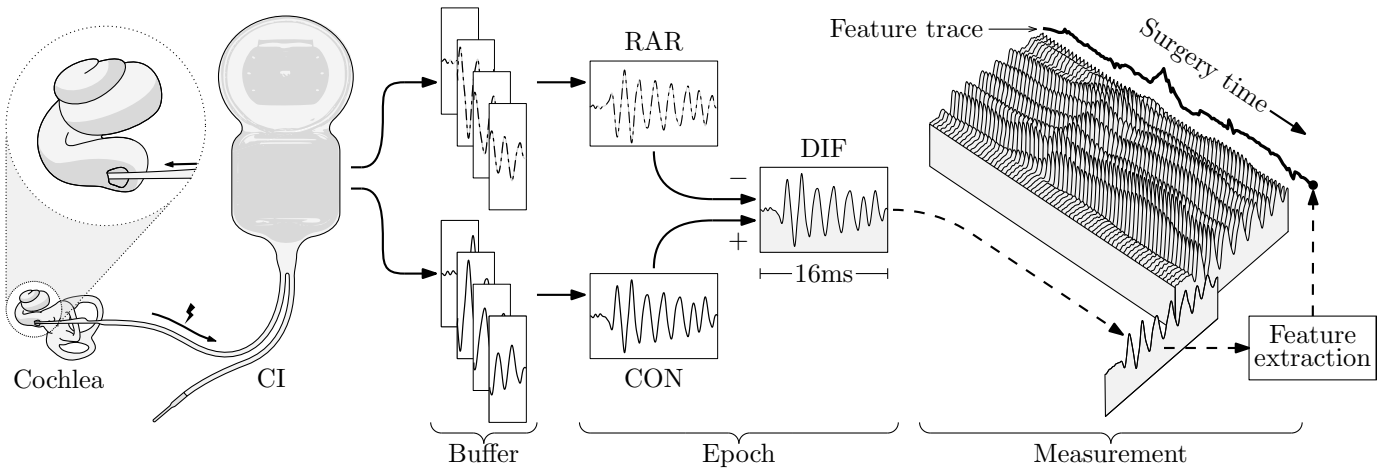


Fig. 1. Schematic overview of a typical intraoperative real-time Electrocochleography (rt-ECochG) measurement. The cochlea generates biopotentials as a response to acoustic stimulation. The rt-ECochG is recorded directly by the cochlear implant (CI) at the most apical intracochlear electrode, which is slowly inserted through the round window. The signal is digitized at a sampling rate  $f_s = 20.5\text{kHz}$  and raw data chunks of a few milliseconds length are buffered before stitched together to form a full response. The time span of a response is denoted an *epoch* and lasts from 11 to 16 milliseconds. A response contains a condensation (CON) and rarefaction (RAR) response pair which result in the difference signal (DIF) after subtraction. The DIF signal is used to analyze the cochlear microphonic (CM), a commonly used component of the ECochG signal. The continuous recording of responses generates a sequence of epochs, which are combined into the rt-ECochG *measurement*. By extracting features from the individual responses, *feature traces* are created over the duration of a measurement, as shown here on the basis of the CM amplitude. We refer to a collection of feature traces as the *insertogram*.

i.e.,

$$\tilde{\kappa}_k = \sum_{p=1}^P \kappa_k^{(p)}, \quad (15)$$

$$\tilde{\xi}_k = \sum_{p=1}^P \xi_k^{(p)}, \quad (16)$$

$$\tilde{W}_k = \sum_{p=1}^P W_k^{(p)}. \quad (17)$$

While each segment in the composite cost has additionally assigned its individual output vector  $c^{(p)}$  and decay factor  $\gamma^{(p)}$ , the transition matrix  $A$  and state vector  $x$  are common for all segments. This simplifies the subsequent computation, but is not a limitation of the method, since ALSSMs can be stacked. To superimpose  $Q$  models, we can apply

$$A = \text{diag} \left( A^{(1)}, \dots, A^{(Q)} \right) \quad (18)$$

$$x = \left[ (x^{(1)})^\top \quad \dots \quad (x^{(Q)})^\top \right]^\top \quad (19)$$

$$c = \left[ c^{(1)} \quad \dots \quad c^{(Q)} \right]. \quad (20)$$

### E. Signal and Event Classification using ALSSMs

Since a cost as in (4), or more generally (14), provides a measure of similarity between a model and the observed signal, we can use the costs to evaluate the performance of several models. We denote the ratio between two such cost remainders a *cost ratio*, which is closely related to the likelihood ratio of two alternative hypotheses in statistics. Since likelihoods are often in logarithmic scale, we analogously introduce the log-cost ratio (LCR)

$$\text{LCR}_k = -\frac{1}{2} \log \frac{\min_{x \in \mathcal{X}_1} J_a^b(x_1, k; \gamma_1)}{\min_{x \in \mathcal{X}_2} J_a^b(x_2, k; \gamma_2)} \in \mathbb{R} \quad (21)$$

with  $\mathcal{X}_1$  and  $\mathcal{X}_2$  being distinct feature spaces [34].

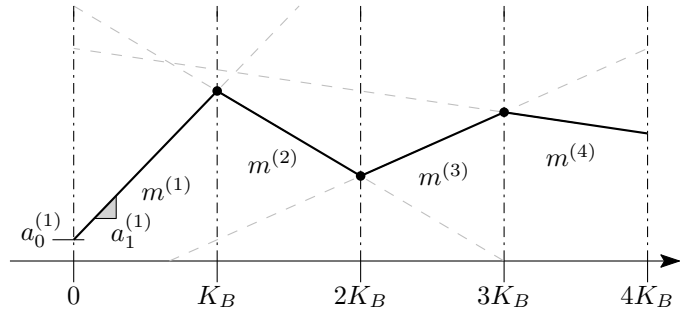


Fig. 2. Model of the amplifier drift artifact naturally occurring in intraoperative real-time Electrocochleography (rt-ECochG) when paralleled by real-time impedance measurements. The line segments are connected at the transition points of subsequent buffer cycles of the analog-to-digital converter.

### F. Artifact Removal in ECochG using ALSSMs

The currents injected by concurrent impedance measurements cause the analog amplifier of the ECochG measurement system to drift. As the polarity of these measurement currents alternate, the resulting drift artifact resembles a stationary triangular wave with the known period of a single buffer cycle. However, the exact slopes of the artifact depend on the electric properties of the surrounding tissue, which are unknown.

To compensate for the drift artifact, we design a piece-wise linear model (cf., Figure 2) of  $Q$  continuous line segments. The model of line segment  $q \in \{1, \dots, Q\}$  is

$$m_i^{(q)}(x) = a_0^{(q)} + a_1^{(q)} i. \quad (22)$$

The model is fitted to the raw measurement signal using a composite cost over the full epoch duration.

165 The ALSSM parametrization for a line model as in (22) is

$$A^{(q)} = \begin{bmatrix} 1 & 1 \\ 0 & 1 \end{bmatrix}, \quad c^{(q)} = [1 \quad 0] \quad (23)$$

166 with state vector

$$x^{(q)} = \begin{bmatrix} a_0^{(q)} & a_1^{(q)} \end{bmatrix}^T, \quad (24)$$

167 where  $a_0$  reflects the line offset and  $a_1$  the slope. A total of  
168  $Q$  ALSSMs are then stacked according to (18)-(20) to obtain  
169 a composite cost (14). Each line model must connect to its  
170 successor, which is provided by the equality constraints

$$m_{qK_B}^{(q)} = m_{qK_B}^{(q+1)} \quad (25)$$

171 with  $K_B$  being the buffer size, i.e., the width of each line  
172 segment in number of samples. The cost segments match the  
173 buffer cycle width. The filter is thus evaluated only once, at  
174  $k = 0$ . The constraints from (25) for  $Q = 4$  are incorporated  
175 by applying (13) with

$$H = \begin{bmatrix} -K_B & K_B & K_B & 3K_B & 1 \\ 1 & 0 & 0 & 0 & 0 \\ 0 & -2K_B & K_B & 3K_B & 1 \\ 0 & 1 & 0 & 0 & 0 \\ 0 & 0 & -3K_B & 3K_B & 1 \\ 0 & 0 & 1 & 0 & 0 \\ 0 & 0 & 0 & 0 & 1 \\ 0 & 0 & 0 & 1 & 0 \end{bmatrix}. \quad (26)$$

176 The window functions are almost rectangular with a decay  
177 factor for reverse recursion  $\gamma_{\leftarrow}^{(q)} = \frac{1000}{1000-1}$ ,  $q \in \{2, \dots, Q\}$ ,  
178 except for the first window, where a slight decay was chosen  
179 with  $\gamma_{\leftarrow}^{(1)} = \frac{0.5K_B}{0.5K_B-1}$  with  $K_B = 60$  to emphasize the pre-  
180 stimulation baseline.

181 With this strategy, the signal is reconstructed by subtracting  
182 the artifact model trajectory from the raw epoch before the  
183 next processing step.

### 184 G. Noise Reduction in DIF using ALSSMs

185 The morphology of a CM response is mainly determined by  
186 the acoustic stimulus [15]. This a priori knowledge enables to  
187 design a specific ALSSM filter that accurately reproduces the  
188 stimulation frequency  $f_0$ . To approximate the CM, we used a  
189 sinusoidal model of the form

$$m_i = \alpha \cdot \cos(\Omega_0 i + \phi) \quad (27)$$

190 with fixed frequency

$$\Omega_0 = 2\pi f_0 / f_s, \quad (28)$$

191 being normalized to the recording sampling rate  $f_s$ . The  
192 estimation parameters  $\alpha$  and  $\phi$  represent the amplitude and  
193 the phase of the sinusoidal. The ALSSM parametrization  
194 equivalent to (27) is

$$A = \begin{bmatrix} \cos \Omega & -\sin \Omega \\ \sin \Omega & \cos \Omega \end{bmatrix}, \quad c = [1 \quad 0] \quad (29)$$

195 with state vector

$$x = \alpha \begin{bmatrix} \sin \phi & \cos \phi \end{bmatrix}^T, \quad (30)$$

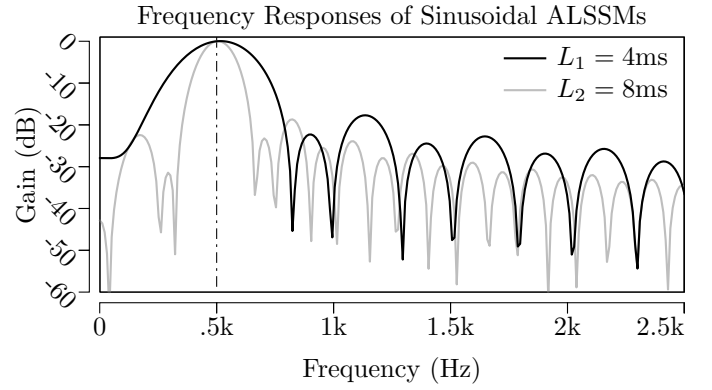


Fig. 3. Frequency responses of a sinusoidal Autonomous Linear State-Space Model (ALSSM) filter with ground frequency  $f_0 = 500\text{Hz}$  and with two different window lengths  $L_1$  and  $L_2$  applying an exponentially decaying window. We note that wider windows (as with  $L_2$ ) provide a higher frequency specificity of the filter.  $L_1 = 4\text{ms}$ ,  $L_2 = 8\text{ms}$ .

cf., table I in [34]. For the composite cost window function, we  
196 chose a symmetric exponential decay with  $\gamma_l$  for  $i = k+a \dots k$   
197 and  $\gamma_r$  for  $i = k+1 \dots k+b$ . By adjusting the length  
198 and window shapes of the cost segment, filters of different  
199 frequency characteristics can be obtained. To form a bandpass  
200 filter, centered around  $f_0$  as shown in Figure 3, our model  
201 can simply be evaluated at  $m_0(x)$  for every filter index  $k$ .  
202 By increasing the window width  $L = b - a$ , we observe the  
203 frequency specificity of the filter will also be increased. To  
204 preserve the frequency specificity of the filters for different  
205 stimulation frequencies, we adapt the window length accord-  
206 ingly.  
207

### 208 H. Morphological Analysis of the CM using ALSSMs

209 The most commonly used feature to assess a CM response is  
210 the amplitude at the  $f_0$ -bin of the amplitude spectrum, obtained  
211 by fast Fourier transform (FFT) to the DIF epoch. In analogy,  
212 we extract the local amplitude and phase estimations  $\hat{\alpha}_k$  and  
213  $\hat{\phi}_k$ , respectively.

214 In a second step, we extract a confidence metric, how well  
215 our model (27) represents the observed data. For this, we  
216 compare the CM model (27) with a noise model by calculating

$$\text{LCR}_k = -\frac{1}{2} \log \frac{\min_{x \in \mathbb{R}^2} (J_a^0(x, k; \gamma_l) + J_1^b(x, k; \gamma_r))}{J_a^0(\mathbf{0}, k; \gamma_l) + J_1^b(\mathbf{0}, k; \gamma_r)} \quad (31)$$

217 according to (21) [35]. Any  $\text{LCR} > 0$  indicates that the CM  
218 model explains the observation locally better than the noise  
219 model. To aggregate the amplitude information of a full epoch,  
220 we calculate an LCR-weighted average of the amplitudes.  
221 In doing so, plausible signal periods are emphasized. We  
222 parameterized the average with a window function (Hamming  
223 window) similar to the FFT to minimize windowing effects.  
224 The per-epoch average amplitude is therefore given by

$$\bar{\alpha} = \sum_{k=0}^K w_k \text{LCR}_k \alpha_k \quad (32)$$



with  $w_i$  being the window function value. In analogy to (32), the per-epoch average

$$\overline{\text{LCR}} = \sum_{k=0}^K w_k \text{LCR}_k \quad (33)$$

is calculated to quantify an entire epoch.

### I. Verification with Simulation Data

To test the suitability of the sinusoidal CM model, we performed a controlled sensitivity analysis of the amplitude estimation algorithm using simulated ECochG signals. Testing with simulation data allows to exclude external disturbances from the analysis and to examine the CM amplitude estimation separately from the artifact removal.

For signal synthesis, we used a verified open-source model of the auditory periphery by Zilany *et al.* [39]–[45]. This model allows to simulate IHC and OHC responses to a user-defined acoustic stimulus. We reproduced three typical ECochG waveforms (A, B and C) as seen during surgery by combining the simulated IHC and OHC cell potentials [45]. For each waveform, we varied the recruitment coefficients  $C_{\text{IHC}}, C_{\text{OHC}} \in [0, 1]$  of IHCs and OHCs as well as the intensity  $I \in \mathbb{R}$  (in  $\text{dB}_{\text{SPL}}$ , sound pressure level SPL) of the 11ms acoustic 500Hz pure-tone stimulus in the simulation. The actual simulation parameters were A:  $I = 60\text{dB}_{\text{SPL}}, C_{\text{IHC}} = C_{\text{OHC}} = 1$ , B:  $I = 110\text{dB}_{\text{SPL}}, C_{\text{IHC}} = C_{\text{OHC}} = 0.5$ , C:  $I = 60\text{dB}_{\text{SPL}}, C_{\text{IHC}} = 0, C_{\text{OHC}} = 1$ . Figure 4 compares real intraoperative rt-ECochG recordings to the simulations. We added artificial pink noise to the signals to simulate different signal-to-noise ratios (SNRs).

For comparison, we also applied a commonly used conventional method on the same data set, which we reproduced to the best of our knowledge [20], [46]. In the conventional method, the discrete amplitude spectrum of the response is calculated using the FFT. The CM amplitude is then estimated using the  $f_0$ -bin of the spectrum's absolute values. To interpolate in frequency domain ( $\Delta f \approx 25\text{Hz}$ ) and minimize leakage, the signal is zero-padded and multiplied with a Hamming window before the FFT. To estimate the noise level and its standard deviation, 3 preceding and 3 succeeding bins, starting 9 bins away from the  $f_0$ -bin are used [20]. With that, we also calculated the  $z$ -score of the  $f_0$ -bin.

We evaluated the performance of the algorithms using Monte Carlo simulations. The test includes estimations of the CM amplitude and an evaluation of response confidence metrics in the DIF signal for the three test waveforms (Figure 4 A-C). In the conventional method, the  $z$ -score was used as the confidence metric. The performances of the different methods were evaluated with 10'000 samples per test waveform with SNRs in the range of  $-10\text{dB}$  to  $+20\text{dB}$ .

### J. Validation with Intraoperative Recordings

For illustration purposes, we applied the algorithms to a few exemplary patient data from an ongoing observational study and present the results graphically. More specifically, the real data presented throughout this paper come from five patients

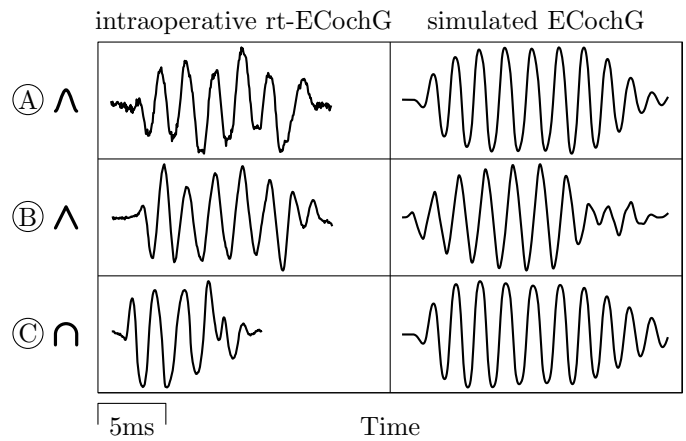


Fig. 4. Comparison of intraoperative real-time electrocochleography (rt-ECochG) responses to simulation data with normalized amplitudes. Shown are the difference signals (DIF) obtained by subtraction of responses from a condensation and rarefaction 500Hz acoustic pure tone stimulus. (A) DIF exhibiting sinusoidal peaks. (B) DIF exhibiting sharp peaks. (C) DIF exhibiting round peaks.

who averaged 59.2 years of age at implantation and had a pure tone average (PTA) of  $76.7\text{dB}_{\text{HL}}$  (hearing level HL).

We recorded rt-ECochG and rt-impedance data from CI patients during electrode insertion. The experimental study has been approved by the local institutional review board *Kantonale Ethikkommission Bern (Cantonal Ethics Committee of Bern)*, Switzerland (BASEC ID 2019-01578) and was conducted in compliance with the Declaration of Helsinki. All participants or their legal guardian gave written informed consent before participating in the study.

Before the surgical incision, we placed a sterile insert foam eartip with a connected sound tube into the patient's external auditory canal [47], [48]. For stimulation, we connected the acoustic unit of a hybrid sound processor (*Nucleus 7*, Cochlear Ltd., Melbourne, Australia) to the sound tube. Prior to insertion, we transcutaneously connected the sterile-packed transmitter coil of the sound processor to the implant. Insertion was then performed with pure tone stimulation and measurement of both rt-ECochG and impedance through the implant (*CI622*, Cochlear Ltd., Melbourne, Australia) using the manufacturer's measurement software (*Cochlear Research Platform 2.0*, Cochlear Ltd., Melbourne, Australia). The applied pure tone stimuli were 11ms long and had an amplitude of either  $100\text{dB}_{\text{HL}}$  for 250Hz or  $108\text{dB}_{\text{HL}}$  for 500Hz. The epochs were recorded unfiltered over a window of 16ms and a sampling rate of 20.5kHz. Impedance data were obtained using the default intraoperative setting of the *Cochlear Research Platform 2.0*, in which the monopolar impedances of all electrodes are measured simultaneously to rt-ECochG. The results of the measurements were not communicated to the surgeon until the insertion was complete. This was done to avoid influencing the insertion process.

We post-processed the collected data using our signal processing pipeline, which includes artifact removal, amplitude estimation, and LCR calculation. For comparison, we recorded the amplitude trace provided by the measurement software

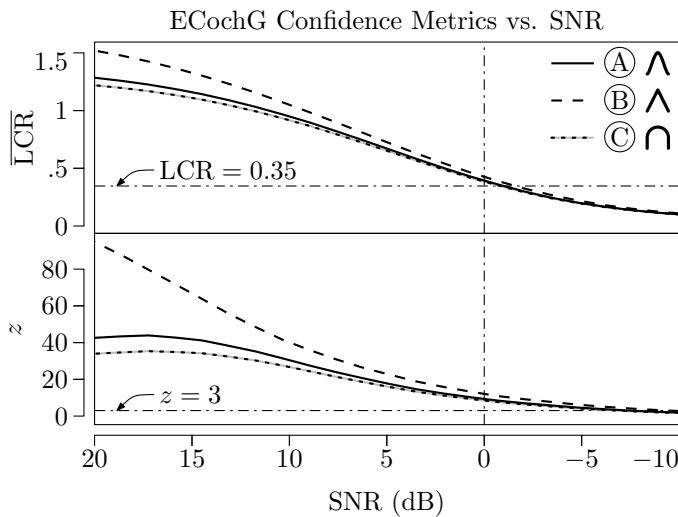


Fig. 5. Evaluation of confidence metrics for electrocochleography (ECoChG) responses in simulation data at different signal-to-noise ratios (SNRs). The curves show mean values for  $n = 10^4$  trials of three characteristic waveforms (Figure 4 A-C) with added random noise. Top panel: Logarithmic cost ratio (LCR) obtained by comparing a localized Autonomous Linear State-Space Model (ALSSM) of the cochlear microphonic (CM) versus a pure noise model. Bottom panel:  $z$ -score obtained by a FFT-based spectral estimation.

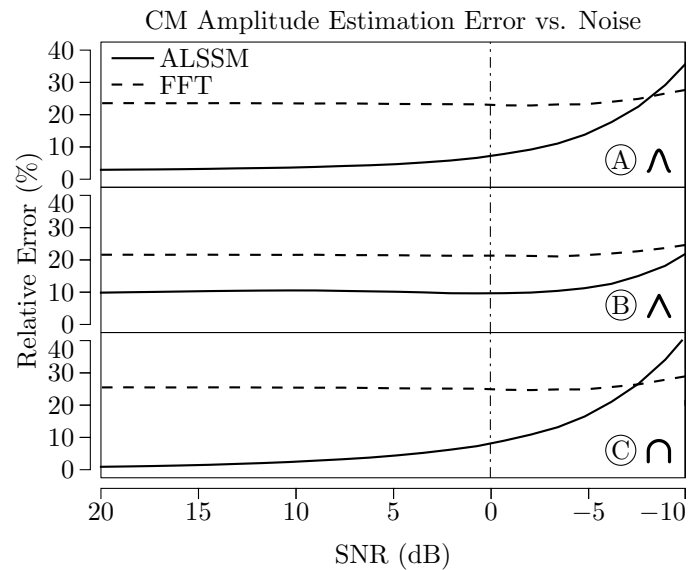


Fig. 6. Absolute errors of cochlear microphonic (CM) amplitude estimations in simulated electrocochleography (ECoChG) data at different signal-to-noise ratios (SNRs). Each panel shows the averaged results for one of three characteristic waveforms (Figure 4 A-C) with added random noise from  $n = 10^4$  trials. For comparison, the CM amplitudes were estimated by the new method using Autonomous Linear State-Space Models (ALSSM) and a conventional algorithm based on the fast Fourier transform (FFT).

312 similar to the conventional method explained in subsection II-I.

### 313 III. RESULTS

#### 314 A. Verification with Simulation Data

315 Figure 5 compares the simulation results of the algorithms  
316 for determining the confidence metric of the CM responses  
317 for the three test waveforms (Figure 4 A-C). The top panel  
318 contains the results for the ALSSM method, while the bot-  
319 tom panel depicts the results of the conventional method.  
320 The curves show that the ALSSM method provides a more  
321 homogeneous result over different CM shapes, especially in  
322 the range of distinct responses with  $\text{SNR} > 0\text{dB}$ .

323 As a first approach to establish a threshold for binary  
324 classification of the presence of physiological responses, we  
325 chose  $\overline{\text{LCR}} > 0.35$ , where the cost of the CM model exceeds  
326 twice the cost of the noise model. As a result, signals for  
327 all test waveforms with  $\text{SNR} > -2\text{dB}$  are being considered  
328 significant. Using the conventional method, on the other hand,  
329 even signals with  $\text{SNR} > -7.5\text{dB}$  (waveforms A and C) and  
330  $\text{SNR} > -10.3\text{dB}$  (waveform B) are considered significant  
331 responses ( $p < 0.01$ ).

332 Figure 6 shows the relative absolute errors of the amplitude  
333 estimation comparing the ALSSM method and the conven-  
334 tional method at different SNRs. Each panel corresponds to  
335 the results of one of the three test waveforms (Figure 4 A-C).

336 The ALSSM estimated the CM amplitude more accurately  
337 in all simulations, and performed particularly well for wave-  
338 forms (A) and (C). Both methods showed the largest error  
339 for waveform (B). The ALSSM method achieved a smaller  
340 error in this case as well. At SNRs  $< -7.5\text{dB}$ , the estimation  
341 error of the ALSSM method is higher than the error of the  
342 conventional method. Since responses with such a low SNR

are not considered significant by either method, the amplitude  
estimates in this range are invalid anyway.

#### 343 B. Validation with Intraoperative Recordings

344 The top panel in Figure 7 shows a raw DIF epoch from a  
345 rt-ECoChG measurement distorted by the artifact as described  
346 in subsection II-F together with the estimated artifact model  
347 trajectory. We reconstructed the signal as described in subsec-  
348 tion II-F (bottom panel). We applied the CM ALSSM (27)  
349 with  $L = 2\text{ms}$  for noise reduction. By using the ALSSM  
350 as a bandpass filter, the transient portions of the signal are  
351 reproduced. Note that the parameters of the localized model  
352 were also estimated at the same time.

353 Figure 8 shows the pipeline result for a 250Hz pure-tone  
354 insertogram (i.e., rt-ECoChG and rt-impedance measurements  
355 from the start of the electrode array insertion until full inser-  
356 tion), with three exemplary DIF epochs of different distortion  
357 and noise levels shown individually. The examples show that  
358 artifacts can be removed applying the artifact model. Further,  
359 the CM model fits well to the observed data within the window  
360 considered for the cost computations.

361 The result is an amplitude trace with artifacts removed,  
362 which at the same time retains its fast features. This becomes  
363 especially evident when comparing the ALSSM amplitude  
364 trace with the amplitude trace obtained using the conventional  
365 method. The intermediate rise in amplitude between 25 and  
366 60 seconds as estimated by the conventional method coincides  
367 with the passage of the apical electrode through the round  
368 window at the start of the insertion (drop in apical impedance  
369  $|Z_{22}|$ ). This is not reproduced by the ALSSM method. Finally,  
370  
371

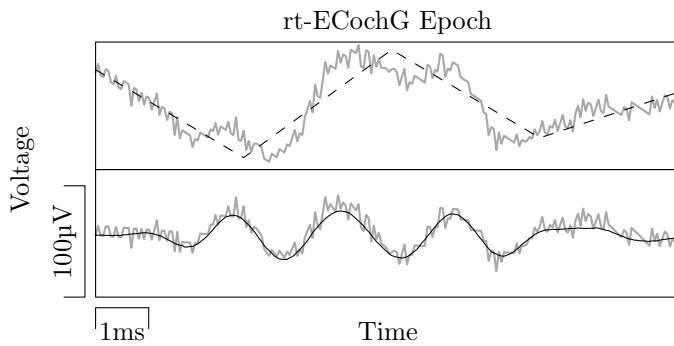


Fig. 7. Epoch from an intraoperative real-time electrocochleography (rt-ECoChG) measurement, distorted by the amplifier drift artifact caused by concurrent real-time impedance measurements before and after application of the Autonomous Linear State-Space Model (ALSSM) filters. Top panel: Raw epoch before processing (*gray*) and artifact estimation (*black dashed*). Bottom panel: Reconstructed signal before (*gray*) and after (*black*) noise reduction.

372 the per-epoch average LCR provides an additional confidence  
373 metric.

374 Impedance traces of the apical (ICE 22) and basal (ICE  
375 01) intracochlear electrodes are shown in the bottom panel  
376 to illustrate the entire insertogram. The impedance of the  
377 apical electrode elevates at 90 seconds, as expected due to the  
378 geometry of the cochlea, but then decreases towards the initial  
379 level [33], [49]–[51]. The impedance of the basal electrode  
380 drops sharply around 155 seconds after entering the fluid filled  
381 scala tympani. This event coincides with a spike in the CM  
382 amplitude estimate of the conventional method. However, this  
383 spike is not visible in the amplitude trace of the ALSSM  
384 method (Figure 8, Epoch C).

#### 385 IV. DISCUSSION

386 We have implemented a signal processing pipeline for real-  
387 time morphological analysis of rt-ECoChG signals. This signal  
388 processing pipeline includes artifact removal (IV-A), noise  
389 reduction (IV-B), and a local model for feature extraction  
390 (IV-C).

##### 391 A. Artifact Removal

392 We demonstrated that artifacts caused by simultaneous rt-  
393 impedance measurements can be removed in rt-ECoChG using  
394 our artifact ALSSM. The model-based approach allows the  
395 discontinuities of the artifact to be adequately represented.  
396 The estimation of the artifact becomes optimal when all other  
397 signal components are offset free over each single buffer cycle.  
398 However, the effects of this requirement are mitigated by  
399 constraining the individual models over the entire epoch. In  
400 addition, common modes of CON and RAR are eliminated  
401 in the DIF signal. In the future, the artifact parameters ob-  
402 tained with our approach potentially allows the derivation of  
403 intracochlear capacitive properties during the recording of an  
404 insertogram.

##### B. Noise Reduction

405 In the example from Figure 7, we showed that the CM  
406 model is suitable for noise reduction in the DIF signal. The  
407 sinusoidal ALSSM behaves like a band-pass filter, which be-  
408 comes less frequency specific when the window is shortened.  
409

##### C. Feature Extraction

410 We used ALSSMs to locally fit a CM model to the observed  
411 data by estimating amplitude and phase. Simultaneously, we  
412 provided a confidence metric about the presence of a physio-  
413 logical response using LCR.  
414

415 The simulations showed that the per-epoch average LCR  
416 yields similar results for all tested waveforms, and therefore  
417 is a more robust confidence metric for signal classification  
418 than the  $z$ -score from the conventional method. Thus, objective  
419 analysis for different rt-ECoChG waveforms is facilitated with  
420 the novel ALSSM method. The steeper slope of the LCR  
421 curves relative to the dynamic range in the region of SNR =  
422 0dB implies a higher resolution of the confidence metric  
423 available for classifying the signals. Our first attempt to find a  
424 suitable threshold for binary classification of responses based  
425 on the LCR still needs refinement, since the classification with  
426 an LCR threshold of 0.35 showed to be rather conservative.

427 With the ALSSM method, the amplitude of simulated CM  
428 could be estimated more accurately than with the conventional  
429 method. The localized CM model provides a more detailed  
430 representation of the amplitudes in a single epoch. By weight-  
431 ing the individual amplitudes in an epoch using LCR, the  
432 per-epoch average amplitude can be estimated more robustly.  
433 The amplitude estimation for both methods could possibly be  
434 improved by considering the harmonics.

435 ECoChG signals exhibit a rich morphology that includes  
436 features such as onset delay, phase, and envelope that could  
437 be used for trauma detection in the future. In a next step,  
438 it will be important to precisely determine these features by  
439 fitting a global CM model. In this context, the LCR and phase  
440 estimation of the CM ALSSM are indispensable [35], [36].

##### D. Study Limitations

441 The main limitation of the current study is the complexity  
442 of the CM model. To obtain a morphological description and  
443 feature set adequate for trauma detection, the full CM must  
444 be fitted with its transient components, in place of a local  
445 model. In addition, the artifact estimation could be improved  
446 by fitting a global CM model simultaneously with the artifact  
447 model, which is feasible with our approach, since ALSSMs  
448 can be stacked. Finally, ECoChG response components other  
449 than the CM such as the auditory nerve neurophonic should  
450 be taken into account for trauma detection, so these must also  
451 be analysed.  
452

453 The simulation data enable the evaluation of new algorithms  
454 for the analysis of intraoperative ECoChG in a controlled  
455 sensitivity analysis. Still, the simulations do not correspond to  
456 complete ECoChG responses, but only reflect the cumulative  
457 cell potentials of the OHC and IHC clusters. To obtain more  
458 vivid ECoChG simulations, a computer model of the cochlea  
459 is required [45].

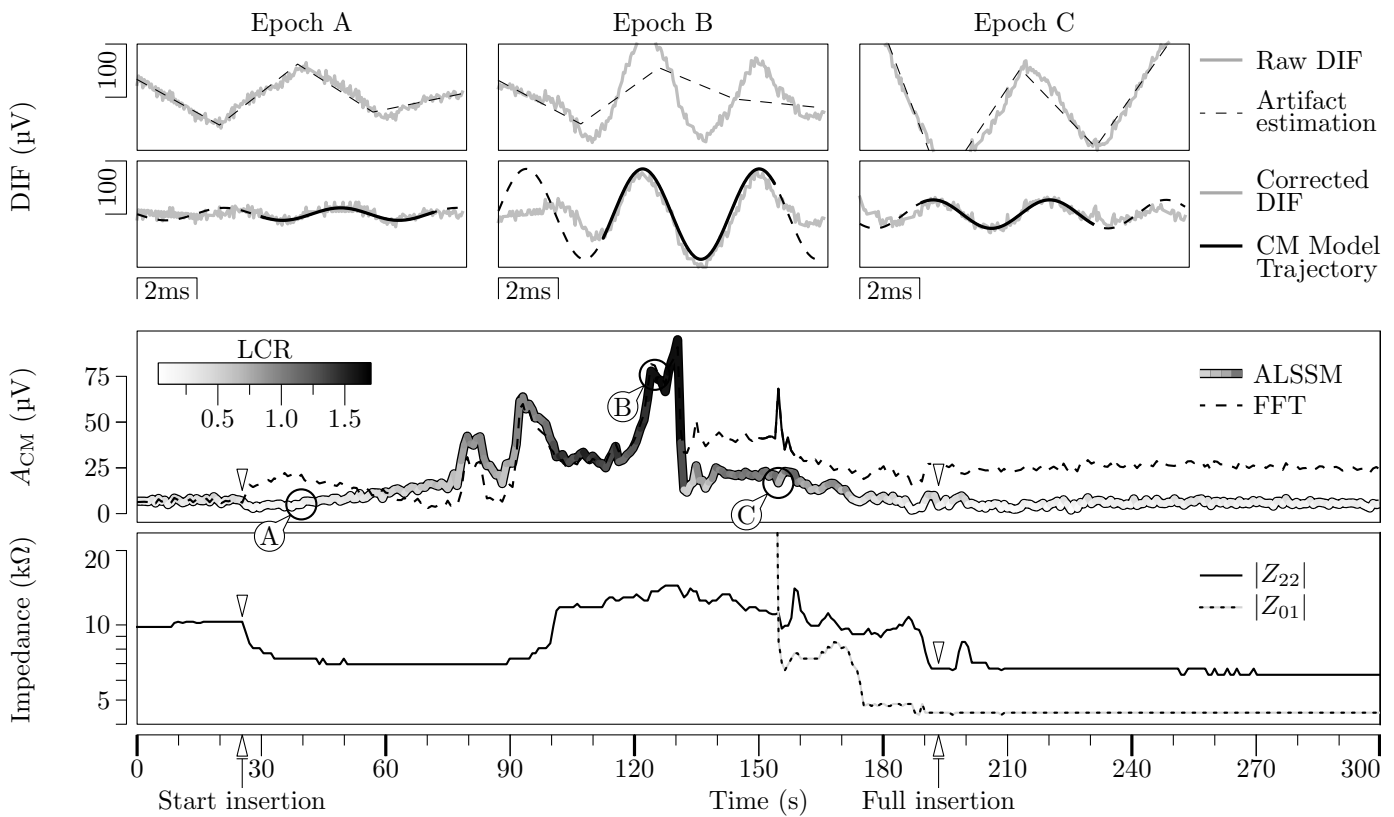


Fig. 8. Intraoperative real-time electrocochleography (rt-ECochG) with concurrent impedance measurements during cochlear implant (CI) electrode insertion. The rt-ECochG signals show the difference (DIF) of the responses obtained from condensation and rarefaction acoustic stimuli. The rt-ECochG was measured directly using the apical intracochlear electrode (ICE) of the CI. Top panels: Raw DIF epochs and artifact estimation using Autonomous Linear State-Space Models (ALSSM). The three epochs represent different groups of observed signals during surgery, namely (A) small response, heavily distorted by the impedance measurements, otherwise small SNR; (B) large response, distorted by the impedance measurements, low SNR; (C) medium response, heavily distorted by the impedance measurements, otherwise medium SNR. Second-top panels: Corrected DIF epochs after artifact removal and trajectories of locally fitted sinusoidal ALSSMs over the cost window width at the location of the maximum logarithmic cost ratio (LCR) representing the cochlear microphonic (CM). *Black, dashed:* Extrapolation of the CM model trajectory over the full epoch. Second-bottom panel: Estimated CM amplitude trace over the course of the CI electrode insertion obtained using the ALSSM method and the  $f_0$ -bin of the FFT. *Gray scale:* Per-epoch average LCR obtained using the ALSSM method. Bottom panel: Clinical impedance traces during CI electrode insertion, obtained from the apical (ICE-22) and basal (ICE-01) intracochlear electrodes.

460 The proposed signal processing pipeline has been illustrated  
 461 by only few intraoperative examples. A prospective study in a  
 462 larger clinical cohort is required to evaluate the classification  
 463 performance of our approach.

## 464 V. CONCLUSIONS

465 We introduced a tool for the analysis of intraoperative real-  
 466 time electrocochleography (rt-ECochG) based on Autonomous  
 467 Linear State-Space Models (ALSSMs). The analysis includes  
 468 artifact removal, noise reduction, and feature extraction to-  
 469 gether with a confidence metric (Logarithmic Cost Ratio,  
 470 LCR) for the physiological response. Our signal processing  
 471 pipeline enables the combination of rt-ECochG with simulta-  
 472 neously recorded impedance data for the purpose of improved  
 473 automated trauma detection during cochlear implantation. We  
 474 tested the feature extraction algorithms in simulated data and  
 475 applied the full signal processing pipeline to a typical intraop-  
 476 erative measurement. The controlled sensitivity analysis with  
 477 simulated data showed that our algorithms performed superior  
 478 to conventional FFT-based methods. With our approach, it

is feasible to perform a robust morphological analysis of  
 the physiological response. Rt-ECochG waveforms can be  
 described more efficiently with ALSSMs than with FFT. The  
 LCR provides the means to automatically decide on the valid-  
 ity of a measured response. Since the presented algorithms are  
 computationally efficient, they could be implemented on the  
 implant itself for future applications other than intraoperative  
 trauma detection, such as cochlear health monitoring while the  
 patient wears the implant.

## REFERENCES

- 488 [1] R. H. Gifford *et al.*, "Cochlear implantation with hearing preservation  
 489 yields significant benefit for speech recognition in complex listening  
 490 environments," *Ear Hear*, vol. 34, no. 4, pp. 413–425, 2013. 491
- 492 [2] S. W. Sheffield *et al.*, "Preserved acoustic hearing in cochlear implanta-  
 493 tion improves speech perception," *J Am Acad Audiol*, vol. 26, no. 2,  
 494 pp. 145–154, Feb 2015. 495
- 496 [3] B. J. Gantz *et al.*, "Preservation of hearing in cochlear implant surgery:  
 497 advantages of combined electrical and acoustical speech processing,"  
 498 *Laryngoscope*, vol. 115, no. 5, pp. 796–802, May 2005. 499
- 500 [4] —, "Review: Clinical perspective on hearing preservation in cochlear  
 501 implantation, the University of Iowa experience," *Hear Res*, p. 108487,  
 502 Mar 2022.



- [5] L. Campbell *et al.*, "Intraoperative Real-time Cochlear Response Telemetry Predicts Hearing Preservation in Cochlear Implantation," *Otol Neurotol*, vol. 37, no. 4, pp. 332–338, Apr 2016.
- [6] D. Bakhos *et al.*, "Electrophysiological exploration of hearing," *European Annals of Otorhinolaryngology, Head and Neck Diseases*, vol. 134, no. 5, pp. 325–331, 2017. [Online]. Available: <https://www.sciencedirect.com/science/article/pii/S1879729617300509>
- [7] C. K. Giardina *et al.*, "Response Changes During Insertion of a Cochlear Implant Using Extracochlear Electrocochleography," *Ear Hear*, vol. 39, no. 6, pp. 1146–1156, 2018.
- [8] A. Dalbert *et al.*, "Assessment of Cochlear Function during Cochlear Implantation by Extra- and Intracochlear Electrocochleography," *Front Neurosci*, vol. 12, p. 18, 2018.
- [9] —, "Simultaneous Intra- and Extracochlear Electrocochleography During Electrode Insertion," *Ear Hear*, vol. 42, no. 2, pp. 414–424, 2021.
- [10] S. Weder *et al.*, "Real time monitoring during cochlear implantation: Increasing the accuracy of predicting residual hearing outcomes," *Otology & Neurotology*, vol. 42, pp. 1030–1036, September 2021. [Online]. Available: [https://journals.lww.com/otology-neurotology/Fulltext/2021/09000/Real\\_Time\\_Monitoring\\_During\\_Cochlear\\_Implantation\\_.16.aspx](https://journals.lww.com/otology-neurotology/Fulltext/2021/09000/Real_Time_Monitoring_During_Cochlear_Implantation_.16.aspx)
- [11] K. Schuerch *et al.*, "Objectification of intracochlear electrocochleography using machine learning," *Front Neurol*, vol. 13, p. 943816, 2022.
- [12] A. Buechner *et al.*, "Clinical experiences with intraoperative electrocochleography in cochlear implant recipients and its potential to reduce insertion trauma and improve postoperative hearing preservation," *PLOS ONE*, vol. 17, no. 4, pp. 1–16, 04 2022. [Online]. Available: <https://doi.org/10.1371/journal.pone.0266077>
- [13] S. Wijewickrema *et al.*, "Automatic analysis of cochlear response using electrocochleography signals during cochlear implant surgery," *PLoS One*, vol. 17, no. 7, p. e0269187, 2022.
- [14] C. Bester *et al.*, "Electrocochleography triggered intervention successfully preserves residual hearing during cochlear implantation: Results of a randomised clinical trial," *Hear Res*, vol. 426, p. 108353, Dec 2022.
- [15] P. Dallos *et al.*, "Cochlear inner and outer hair cells: functional differences," *Science*, vol. 177, no. 4046, pp. 356–358, Jul 1972.
- [16] P. Dallos and M. A. Cheatham, "Production of cochlear potentials by inner and outer hair cells," *J Acoust Soc Am*, vol. 60, no. 2, pp. 510–512, Aug 1976.
- [17] S. O'Leary *et al.*, "Monitoring cochlear health with intracochlear electrocochleography during cochlear implantation: Findings from an international clinical investigation," *Ear and Hearing*, 9900. [Online]. Available: [https://journals.lww.com/ear-hearing/Fulltext/9900/Monitoring\\_Cochlear\\_Health\\_With\\_Intracochlear.73.aspx](https://journals.lww.com/ear-hearing/Fulltext/9900/Monitoring_Cochlear_Health_With_Intracochlear.73.aspx)
- [18] J. H. Barnes *et al.*, "Electrocochleography in cochlear implantation: Development, applications, and future directions," *World Journal of Otorhinolaryngology - Head and Neck Surgery*, vol. 7, no. 2, pp. 94–100, 2021, new Insights in Otology and Neurotology. [Online]. Available: <https://www.sciencedirect.com/science/article/pii/S2095881120300536>
- [19] C. K. Giardina *et al.*, "Intracochlear Electrocochleography: Response Patterns During Cochlear Implantation and Hearing Preservation," *Ear Hear*, vol. 40, no. 4, pp. 833–848, 2019.
- [20] D. C. Fitzpatrick *et al.*, "Round window electrocochleography just before cochlear implantation: relationship to word recognition outcomes in adults," *Otol Neurotol*, vol. 35, no. 1, pp. 64–71, Jan 2014.
- [21] T. E. Fontenot *et al.*, "A Model-Based Approach for Separating the Cochlear Microphonic from the Auditory Nerve Neurophonic in the Ongoing Response Using Electrocochleography," *Front Neurosci*, vol. 11, p. 592, 2017.
- [22] B. Krüger *et al.*, "Amplitude growth of intracochlear electrocochleography in cochlear implant users with residual hearing," *J Acoust Soc Am*, vol. 147, no. 2, p. 1147, 02 2020.
- [23] K. Koka *et al.*, "Electrocochleography in Cochlear Implant Recipients With Residual Hearing: Comparison With Audiometric Thresholds," *Ear Hear*, vol. 38, no. 3, pp. e161–e167, 2017.
- [24] M. S. Harris *et al.*, "Patterns Seen During Electrode Insertion Using Intracochlear Electrocochleography Obtained Directly Through a Cochlear Implant," *Otol Neurotol*, vol. 38, no. 10, pp. 1415–1420, 12 2017.
- [25] L. Sijgers *et al.*, "Simultaneous Intra- and Extracochlear Electrocochleography During Cochlear Implantation to Enhance Response Interpretation," *Trends Hear*, vol. 25, p. 2331216521990594, 2021.
- [26] S. Weder *et al.*, "Toward a better understanding of electrocochleography," *Ear and Hearing*, vol. 41, pp. 1560–1567, November/December 2020. [Online]. Available: [https://journals.lww.com/ear-hearing/Fulltext/2020/11000/Toward\\_a\\_Better\\_Understanding\\_of.13.aspx](https://journals.lww.com/ear-hearing/Fulltext/2020/11000/Toward_a_Better_Understanding_of.13.aspx)
- [27] Y. Dong *et al.*, "Detection of Translocation of Cochlear Implant Electrode Arrays by Intracochlear Impedance Measurements," *Ear Hear*, vol. 42, no. 5, pp. 1397–1404, 2021.
- [28] W. Wimmer *et al.*, "Cochlear Implant Electrode Impedance as Potential Biomarker for Residual Hearing," *Front Neurol*, vol. 13, p. 886171, 2022.
- [29] C. Bester *et al.*, "Four-point impedance as a biomarker for bleeding during cochlear implantation," *Sci Rep*, vol. 10, no. 1, p. 2777, 02 2020.
- [30] C. Shaul *et al.*, "Electrical impedance as a biomarker for inner ear pathology," *Otology & Neurotology*, vol. 40, pp. 518–526, June 2019. [Online]. Available: [https://journals.lww.com/otology-neurotology/Fulltext/2019/06000/Electrical\\_Impedance\\_as\\_a\\_Biomarker\\_for\\_Inner\\_Ear.16.aspx](https://journals.lww.com/otology-neurotology/Fulltext/2019/06000/Electrical_Impedance_as_a_Biomarker_for_Inner_Ear.16.aspx)
- [31] J. Choi *et al.*, "Electrode Impedance Fluctuations as a Biomarker for Inner Ear Pathology After Cochlear Implantation," *Otol Neurotol*, vol. 38, no. 10, pp. 1433–1439, 12 2017.
- [32] S. Schraivogel *et al.*, "Postoperative impedance-based estimation of cochlear implant electrode insertion depth," *Ear and Hearing*, 2023, Ahead-of-print (online).
- [33] F. A. Di Lella *et al.*, "Measuring the electrical status of the bionic ear. re-thinking the impedance in cochlear implants," *Frontiers in Bioengineering and Biotechnology*, vol. 8, 2020. [Online]. Available: <https://www.frontiersin.org/article/10.3389/fbioe.2020.568690>
- [34] R. A. Wildhaber *et al.*, "Windowed state-space filters for signal detection and separation," *IEEE Transactions on Signal Processing*, vol. 66, no. 14, pp. 3768–3783, 2018.
- [35] E. Ren *et al.*, "Real-time interaural time delay estimation via onset detection," in *ICASSP 2021 - 2021 IEEE International Conference on Acoustics, Speech and Signal Processing (ICASSP)*, 2021, pp. 4555–4559.
- [36] F. Waldmann *et al.*, "Onset detection of pulse-shaped bioelectrical signals using linear state space models," *Current Directions in Biomedical Engineering*, vol. 8, no. 2, pp. 101–104, 2022. [Online]. Available: <https://doi.org/10.1515/cdbme-2022-1027>
- [37] R. A. Wildhaber *et al.* (2022) lmlib - an open source model-based signal processing library. [Online]. Available: <https://lmlib.ch/>
- [38] Zalmi, Nour, "A state space world for detecting and estimating events and learning sparse signal decompositions," Ph.D. dissertation, ETH Zurich, 2017. [Online]. Available: <https://doi.org/10.3929/ethz-b-000176652>
- [39] M. S. Zilany and I. C. Bruce, "Modeling auditory-nerve responses for high sound pressure levels in the normal and impaired auditory periphery," *J Acoust Soc Am*, vol. 120, no. 3, pp. 1446–1466, Sep 2006.
- [40] M. S. Zilany *et al.*, "Updated parameters and expanded simulation options for a model of the auditory periphery," *J Acoust Soc Am*, vol. 135, no. 1, pp. 283–286, Jan 2014.
- [41] L. H. Carney, "A model for the responses of low-frequency auditory-nerve fibers in cat," *J Acoust Soc Am*, vol. 93, no. 1, pp. 401–417, Jan 1993.
- [42] X. Zhang *et al.*, "A phenomenological model for the responses of auditory-nerve fibers: I. Nonlinear tuning with compression and suppression," *J Acoust Soc Am*, vol. 109, no. 2, pp. 648–670, Feb 2001.
- [43] I. C. Bruce *et al.*, "An auditory-periphery model of the effects of acoustic trauma on auditory nerve responses," *J Acoust Soc Am*, vol. 113, no. 1, pp. 369–388, Jan 2003.
- [44] —, "A phenomenological model of the synapse between the inner hair cell and auditory nerve: Implications of limited neurotransmitter release sites," *Hear Res*, vol. 360, pp. 40–54, 03 2018.
- [45] M. J. van Gendt *et al.*, "Simulating intracochlear electrocochleography with a combined model of acoustic hearing and electric current spread in the cochlea," *J Acoust Soc Am*, vol. 147, no. 3, p. 2049, 03 2020.
- [46] M. Forgues *et al.*, "Distinguishing hair cell from neural potentials recorded at the round window," *J Neurophysiol*, vol. 111, no. 3, pp. 580–593, Feb 2014.
- [47] K. Schuerch *et al.*, "Increasing the reliability of real-time electrocochleography during cochlear implantation: a standardized guideline," *Eur Arch Otorhinolaryngol*, vol. 279, no. 10, pp. 4655–4665, Oct 2022.
- [48] —, "Performing Intracochlear Electrocochleography During Cochlear Implantation," *J Vis Exp*, no. 181, 03 2022.
- [49] P. Aebischer *et al.*, "Intraoperative impedance-based estimation of cochlear implant electrode array insertion depth," *IEEE Transactions on Biomedical Engineering*, vol. 68, no. 2, pp. 545–555, 2021.
- [50] F. A. Di Lella *et al.*, "In Vivo Real-time Remote Cochlear Implant Capacitive Impedance Measurements: A Glimpse Into the Implanted Inner Ear," *Otol Neurotol*, vol. 40, no. 5S Suppl 1, pp. S18–S22, 06 2019.

- 652 [51] C. K. Giardina *et al.*, "Impedance measures during in vitro cochlear im-  
653 plantation predict array positioning," *IEEE Transactions on Biomedical*  
654 *Engineering*, vol. 65, no. 2, pp. 327–335, 2018.